



# High-temperature oxidation resistance of sputtered (Al,Cr,Nb,Ta,Ti,Si) N coatings

Andreas Kretschmer, Paul Heinz Mayrhofer\*

TU Wien, Institute of Materials Science and Technology E308, Gumpendorferstrasse 7, Vienna 1060, Austria

## ARTICLE INFO

### Keywords:

A ceramic  
A sputtered films  
B TEM  
B SEM  
B XRD  
C oxidation

## ABSTRACT

High-entropy metal-sublattice (Al,Cr,Nb,Ta,Ti)N coatings, with up to 15.0 at% additional Si content were developed and investigated for their oxidation resistance by exposing them for 3, 30, and 100 h to ambient air at 900, 950, and 1000 °C. The Si-free coating is rapidly oxidized, but all of the Si-alloyed coatings survive even the harshest oxidation test. The oxides crystallize mostly in the rutile structure with some Ta<sub>2</sub>O<sub>5</sub>-type phase fractions at higher Si contents. Detailed TEM investigations reveal a varied microstructure across the oxide scales with a succession of Cr-, Al, and Ti-rich top oxide layers, which agrees with a reported thermodynamical calculation of oxide stabilities.

## 1. Introduction

Hard PVD coatings are used to protect underlying substrates like cutting tools or aerospace engine components from wear and oxidative attack in their harsh service environments. In order to reduce service intervals and the use of cutting fluids with negative environmental impact, coatings with higher oxidation resistance are needed to withstand the resulting higher temperatures [1,2]. PVD nitrides are widely used in this context due to a combination of high hardness and thermal stability and their relatively simple reactive deposition using metallic targets. The first developed model system TiN fares rather poor in oxidative environments, already failing in a temperature range around 500 °C [3]. This was significantly improved by forming a solid solution with Al [4], making use of the protective nature of Al<sub>2</sub>O<sub>3</sub>. This improved oxidation resistance is one of the reasons for the economical success of (Al,Ti)N coatings. Cr can substitute Ti for an improved oxidation resistance [5], forming a second branch of widely applied (Al,Cr)N coatings.

Further improvements of the oxidation resistance can be realized with other element additions. One notable example is Ta [6,7], which acts by promoting the direct formation of rutile-structured TiO<sub>2</sub> scales and suppressing the intermediate anatase phase during oxidation [8]. This highlights the importance of phase evolution during oxidation to form protective scales.

The oxidation proceeds faster in the presence of defects that enable fast diffusion of constituents. The most dominant defects in this regard for PVD coatings are the grain boundaries which usually provide a direct

straight path from the substrate throughout the whole coating due to the columnar microstructure. Correspondingly developing fast diffusion pathways within the growing oxide scales on such coatings can be hindered by doping the coating with small amounts of reactive elements like Y [9,10], La [11], and Ce [12] that occupy grain boundaries and block them for the diffusing species.

Next to Al and Cr, Si also forms a protective oxide scale, making it a useful addition to nitride coatings [13]. As SiN is not very miscible with TiN, it forms an amorphous grain boundary phase instead, leading to nano-composite and eventually amorphous coatings at sufficiently high Si contents [14]. These amorphous regions are devoid of any fast diffusion channels, and therefore improve the oxidation resistance tremendously. Musil et al. [15] demonstrated how amorphous nitrides outperform crystalline nitrides in oxidative environments at very high temperatures. But also in the crystalline regime, Si improves the oxidation resistance of TiN [16], (Al,Ti)N [17,18], and (Al,Cr)N [19].

These developments eventually lead to more complex nitrides like (Al,Si,Ta)N [20], or (Al,Cr,Si,Ti)N and (Al,Cr,Si,Ti)O-N [21], culminating eventually in the nitrides of compositionally complex or high-entropy alloys. Among the latter group, rather few investigations of high-temperature oxidation resistance are published despite the large attention given to such PVD nitrides in general. The investigated material systems include (Al,Cr,Ti,V)N [22], (Al,Cr,Ti,V,Zr)N [23], (Hf,Ta,Ti,W,Zr)N [24], and (Al,Hf,Ta,Ti,Zr)N [25]. Despite their general good thermal stability, these coatings were not especially protective in oxidative environments compared to simpler nitrides, and the exposure

\* Corresponding author.

E-mail addresses: [andreas.kretschmer@tuwien.ac.at](mailto:andreas.kretschmer@tuwien.ac.at) (A. Kretschmer), [paul.mayrhofer@tuwien.ac.at](mailto:paul.mayrhofer@tuwien.ac.at) (P.H. Mayrhofer).

to hot air was limited to a few hours at most. An exception is the early work by Shen et al. [26], who studied (Al,Cr,Nb,Si,Ti)N coatings with very good oxidation resistance, here the harshest test condition was 10 h at 1000 °C in air.

This study motivated us in the past to investigate the influence of Si addition on the oxidation resistance of (Al,Cr,Nb,Ta,Ti)N thin films at 850 °C for 100 h [27], varying the Si content between 0 and 15.0 at%. This temperature was chosen to compare our results to similar reported crystalline nitrides like (Al,Ti)N and (Al,Ti,Ta)N that were tested under comparable conditions [28,29]. The results clearly showed that Si is a game-changer for this system, densifying the oxide scale and changing the oxidation rate from a parabolic law to a logarithmic one, nearly halting oxidation after forming a 300 nm thick oxide scale. The Si-alloyed coatings outclassed the (Al,Ti)N and (Al,Ti,Ta)N coatings [28, 29], that were taken as reference. But the different Si contents had no discernible impact on the oxidation resistance in our study, as the test conditions were clearly not harsh enough. In order to study the influence of Si on the high-temperature oxidation, and to push this exceptional material to its limits, we scanned the oxidation behavior in 50 °C increments in the present contribution by subjecting the same coatings to oxidation tests at 900, 950, and 1000 °C for up to 100 h and studied the evolving oxide scales by X-ray diffraction and electron microscopy.

## 2. Methods

We used our magnetron sputtered samples from our previous study [27] for our renewed oxidation test, details on the deposition procedure and coating properties are discussed there. We placed coatings on ( $\bar{1}\bar{1}02$ ) oriented sapphire with 0, 6.4, 9.8, and 15.0 at% Si into a pre-heated furnace with ambient air at 900, 950, and 1000 °C and extracted one sample each after 3, 30, and 100 h from the hot zone, cooling the samples down to room temperature within a few minutes. The phase composition was measured by X-ray diffraction (XRD) using a PANalytical XPert Pro MPD ( $\theta$ - $\theta$  diffractometer) equipped with a Cu-K $\alpha$  source ( $\lambda = 0.15408$  nm, 45 kV and 40 mA) in Bragg-Brentano geometry. The oxidation front was monitored by embedding the samples in a conductive resin, polishing the cross-sections, and observing the cross-sections in a Zeiss Sigma 500 scanning electron microscope (SEM) with a field emission gun (FEG), operated at 10 kV in backscatter electron mode. Transmission electron microscopy (TEM) was performed

with a FEI TECNAI F20, equipped with a FEG, operated at 200 kV. The chemical composition was measured by energy-dispersive X-ray spectroscopy (EDS) linescans and mappings.

## 3. Results and discussion

### 3.1. XRD analysis and SEM cross-sections

The phase evolution of the oxidized samples after 100 h at the different temperatures (data of as deposited and oxidized at 850 °C coatings was shown before in [27]) are presented in Fig. 1 with increasing Si content from left to right. The sapphire substrate occupies the region between 50 and 55°, with a visible spectral line at 47.5°. In some measurements the substrate peak is not visible due to minuscule accidental tilting of the samples, which affects only the single-crystal reflection significantly. The Si-free coating displays a (200) texture in as deposited state. A rutile phase formed during oxidation with the strongest reflections coming from the (101), (002), and (301) planes. (200) and (111) reflections become visible at the higher temperatures. After oxidation at 900 °C, the coating is not visible in the XRD anymore, hinting at complete oxidation.

The sample with 6.4 at% Si shows a weak (200) and stronger (311) texture in as deposited state. Again, a pronounced rutile phase formation is present due to the oxidation, with the (101) and (301) reflections dominating. There are also first signs of an additional Ta<sub>2</sub>O<sub>5</sub>-type phase forming at high temperatures. Due to the large variation of oxides within this element space and their sometimes low symmetry, as well as the clearly present texture even in the oxide scale, it is not possible to identify all the oxide phases uniquely. Instead we show here a small selection of reference lines for an orthorhombic Ta<sub>2</sub>O<sub>5</sub> (which likely contains other metals as well) that could explain the observed reflections.

The sample with 9.8 at% Si exhibits a pronounced (200) texture in as deposited state, that remains up to 1000 °C. The rutile phase forms again with preferred (101) and (301) orientations, but starting at 900 °C, an additional phase forms as indicated by the reflex at 47°. This could be a Ta<sub>2</sub>O<sub>5</sub> phase with strong (002) orientation, but can also be explained as a TaSi<sub>2</sub>-type phase with (112) orientation. It is impossible to determine this from a single peak, but since the same reflection is present also in the sample with the highest Si content, a silicide phase could also be

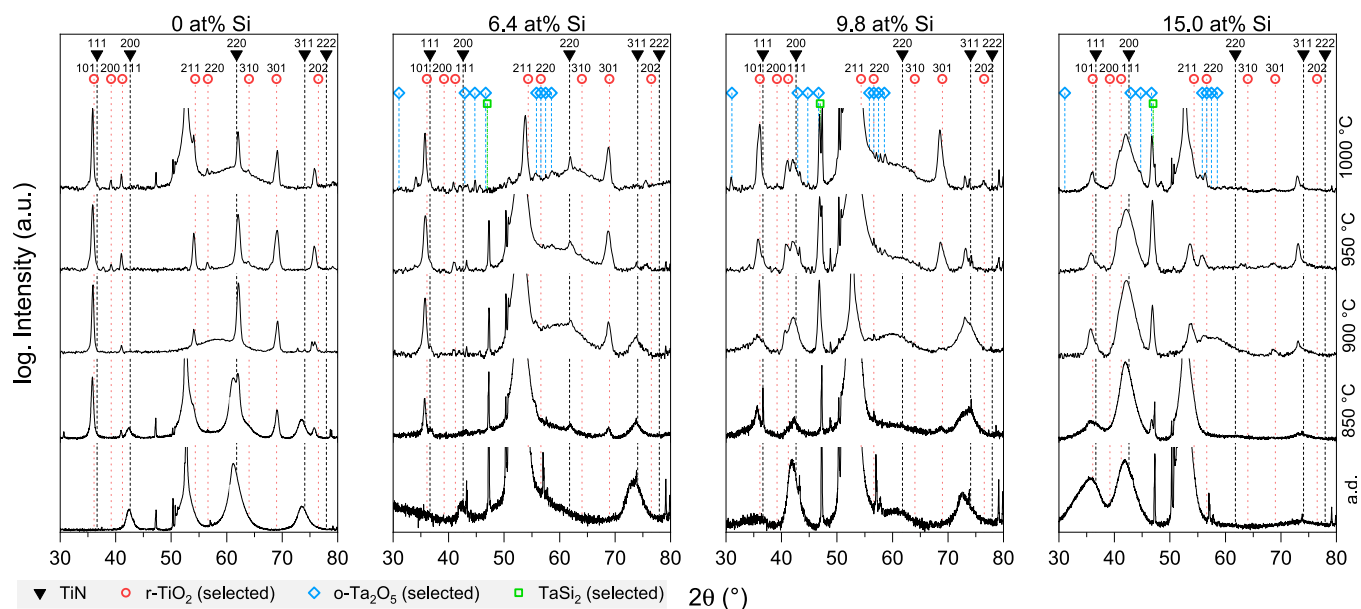


Fig. 1. X-ray diffractograms of the coatings after 100 h oxidation at different temperatures. Only a small selection of reflections is shown for the Ta<sub>2</sub>O<sub>5</sub> and TaSi<sub>2</sub> phases for better visibility. PDF numbers: TiN 00–038–1420, TiO<sub>2</sub> 00–021–1276, Ta<sub>2</sub>O<sub>5</sub> 00–025–0922, TaSi<sub>2</sub> 00–038–0483.

plausible.

The coating with 15.0 at% Si shows a mixed (111) and (200) texture in as deposited state, which becomes a dominant (200) texture after the oxidation tests. Again, the rutile phase evolves, and at least one other oxide phase, but in this sample the nitride signal remains dominant even

after oxidation at 1000 °C, indicating a better oxidation resistance.

The cross-sections of the individual oxide fronts give details on the growth morphology and composition, see the SEM image in Fig. 2 (from left to right with increasing Si content of the coating, and from top to bottom the three temperature groups with 3, 30, and 100 h oxidation

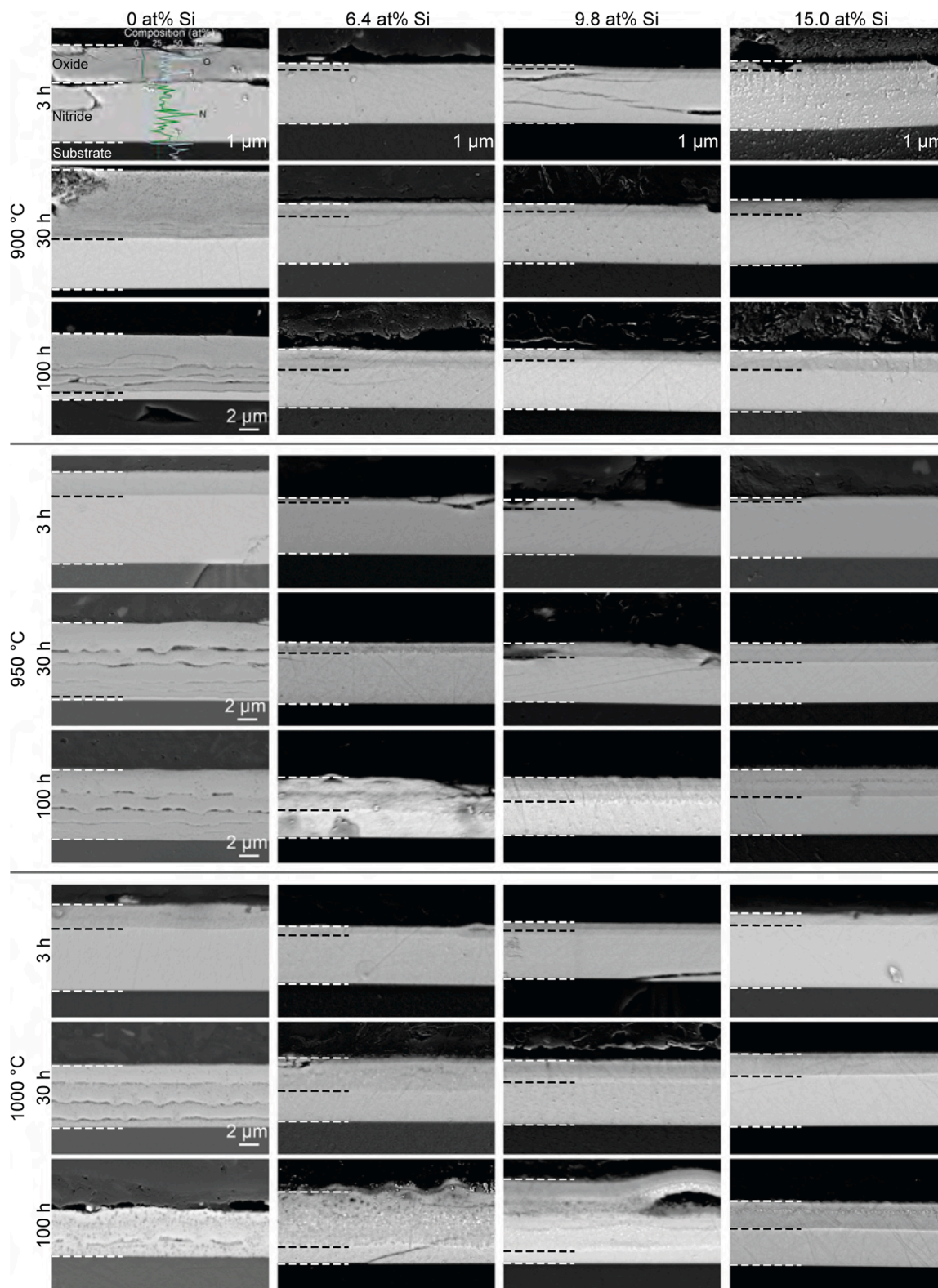


Fig. 2. BSE images of polished cross-sections of the oxidized coatings. An EDS linescan in the top-left shows the distribution of N and O across the cross-section. The 1 μm scalebars apply to all micrographs below, except, where a different scalebar is shown.

time in each). In the back scattered electron (BSE) signal, the substrate on the bottom of the micrographs appears dark just like the embedding resin at the top. The nitride appears lighter compared to the oxide, reflecting the change in the stoichiometry between the heavy metals and the light nonmetals from roughly 1:1 in the nitride to roughly 1:2 as indicated by the rutile phase from XRD investigations, if not even more. The individual regions are separated by dashed lines. This image is meant to provide an overview, larger images can be found in the supplementary materials, while detailed characterization was done by TEM.

The Si-free coating is severely attacked by the oxidative environment even at 900 °C, after 100 h barely any nitride is left, explaining the loss of signal during XRD studies at this point. At the higher temperatures, 30 h are sufficient to completely oxidize this coating. The spallation of individual sub-layers results in a partial delamination of the oxide scale after 100 h at 1000 °C.

The oxidation resistance is much improved when alloying the coating with 6.4 at% Si, with a well-adherent oxide scale with SEM-visible pore-formation only present after 100 h at 950 and 1000 °C.

In contrast to our previous study [27], the harsher oxidation treatments here yield an impact of the different Si contents. The coating with 9.8 at% Si displays similar oxide scale thicknesses compared to the coating with less Si. Only after 100 h at the highest temperature the oxide scale morphology is significantly different, even though the thicknesses are similar. The oxide scale with more Si appears more compact, yet also here do we see sublayers with a less dense region in the center. In both samples, there are still a few 100 nm of nitride coating left after the harshest oxidation conditions.

The coating with 15.0 at% Si stands out against its competitors, forming dense, well-adherent oxide scales that grow only slowly, so that after 100 h at 1000 °C still more than half of the nitride is left.

To gain understanding of the oxidation process we fitted the oxide

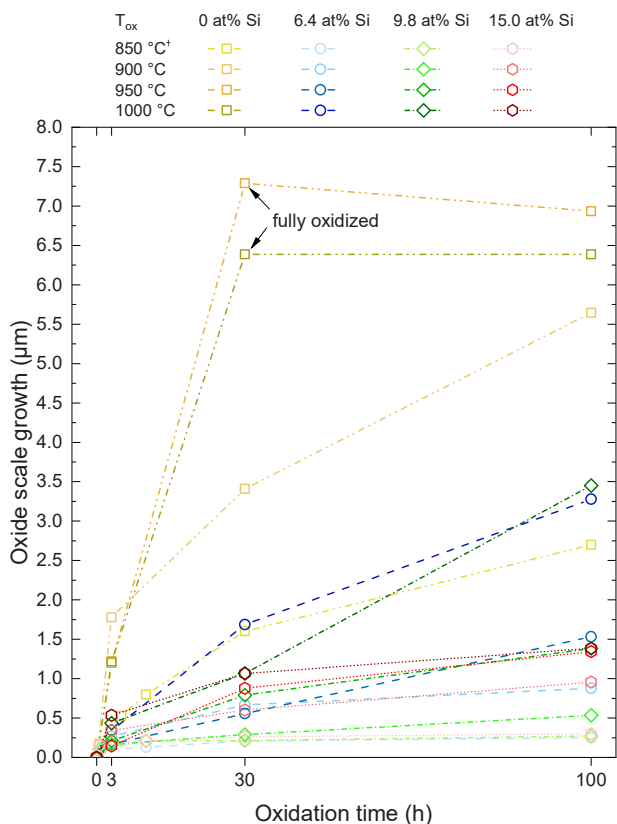


Fig. 3. Oxide growth with time for the different Si contents. A detailed overview with attempted rate law fits can be seen in the supplementary materials. † Data for 850 °C is taken from [27].

growth against time by different rate laws. The oxide growth kinetic, by plotting the measured oxide scale thickness against the oxidation time, Fig. 3, shows that not all the data can be fitted with the same rate law. The different series can be best described with parabolic, cubic, or – for the highest Si content – even with logarithmic laws. For the highest temperature, not the entire series could be fitted with such laws, because the oxidation rate seemingly increases between 30 and 100 h, as the oxide scale becomes less dense during that time period. The attempts at fitting the oxide scale growth are presented in the Supplementary Material.

### 3.2. TEM analysis

More detailed investigations of the oxide scale are conducted by TEM of the coatings with 6.4, 9.8, and 15.0 at% Si, oxidized at 1000 °C for 100 h. The sample with the lowest Si content, presented in Fig. 4, still exhibits a columnar microstructure of the nitride (with remaining 750 nm thickness), Fig. 4a) (overview of the whole cross-section from the substrate on the right, to the top-most oxide layer on the left). The selected area electron diffraction (SAED) pattern from area I yields a single phase fcc structure even after the very long heat treatment at 1000 °C. This can partly be rationalized with the out-diffusion of Al towards the surface, presented in the STEM analysis later, thus stabilizing the fcc structure by leaving the fcc-nitride forming metals behind. At the edge of the nitride layer, oxide columns grow that neatly extend the nitride columns with column diameters around 40 nm. Magnified views of this transition are given in Fig. 4b) and c). The oxide scale columns are roughly 500 nm long before a more equiaxed grain morphology develops. SAED from area II shows a spotty ring pattern, which mostly belongs to a rutile structure, while some additional spots could stem from a Ta<sub>2</sub>O<sub>5</sub> phase, being clearly the minority in this region.

The crack parallel to the surface (to the left of area II) originated from the TEM sample preparation and not from the oxidation itself, as confirmed with the SAED from region III, which shows a similar pattern like region II. Detailed investigations of the area with a globular grain structure, see Fig. 4d), exhibit an average size of roughly 30 nm. Towards the surface of the oxide scale, the grain morphology and chemical composition changes again, see the detail presented in Fig. 4e). The lighter bright-field contrast suggests that the top-most layer is comprised of lighter elements, specifically Al and Ti, than the layer below, leading to a rough surface comprised of significantly larger grains. For a detailed analysis of chemical species throughout the oxide scale we refer to the STEM analysis below, also with significantly larger grains, leading to a rather rough surface. These large grains in this outer region may be a consequence of lighter elements there, which would presumably carry a lower activation energy for diffusion and grain growth with them. The light area beyond these grains is comprised of amorphous carbon, which stems from the embedding resin and is not part of the sample. Also, oxide phases with higher O-content are present in the top-most region, like indicated by the SAED from area IV. This SAED was recorded with a finer aperture, revealing mostly a single-crystal pattern that can be fitted with a Ta<sub>2</sub>O<sub>5</sub> type phase (space group 15), which is different from the XRD results. The remaining spots stem from at least a second crystal within the region covered by the aperture and point towards a rutile structure. The rather complex chemical environment from the high-entropy metal-sublattice nitride will result easily in a local chemical and structural variation in the oxide scale. A high-resolution TEM image of the marked area in Fig. 4e) is shown in Fig. 4f) with a Fast Fourier Transformation (FFT) of the crystalline area in the inset, indicating a different Ta<sub>2</sub>O<sub>5</sub> phase (space group 145). However, this limited sample size does not allow to generally conclude that the crystal structure is different at the top than within the lower region of the oxide scale.

The scanning-TEM (STEM) overview of the sample, Fig. 4g), gives a good gauge of the density and chemical composition. The Al<sub>2</sub>O<sub>3</sub> substrate appears dark as it is comprised of very light elements, then comes the light and dense nitride layer, beyond which the columnar part of the

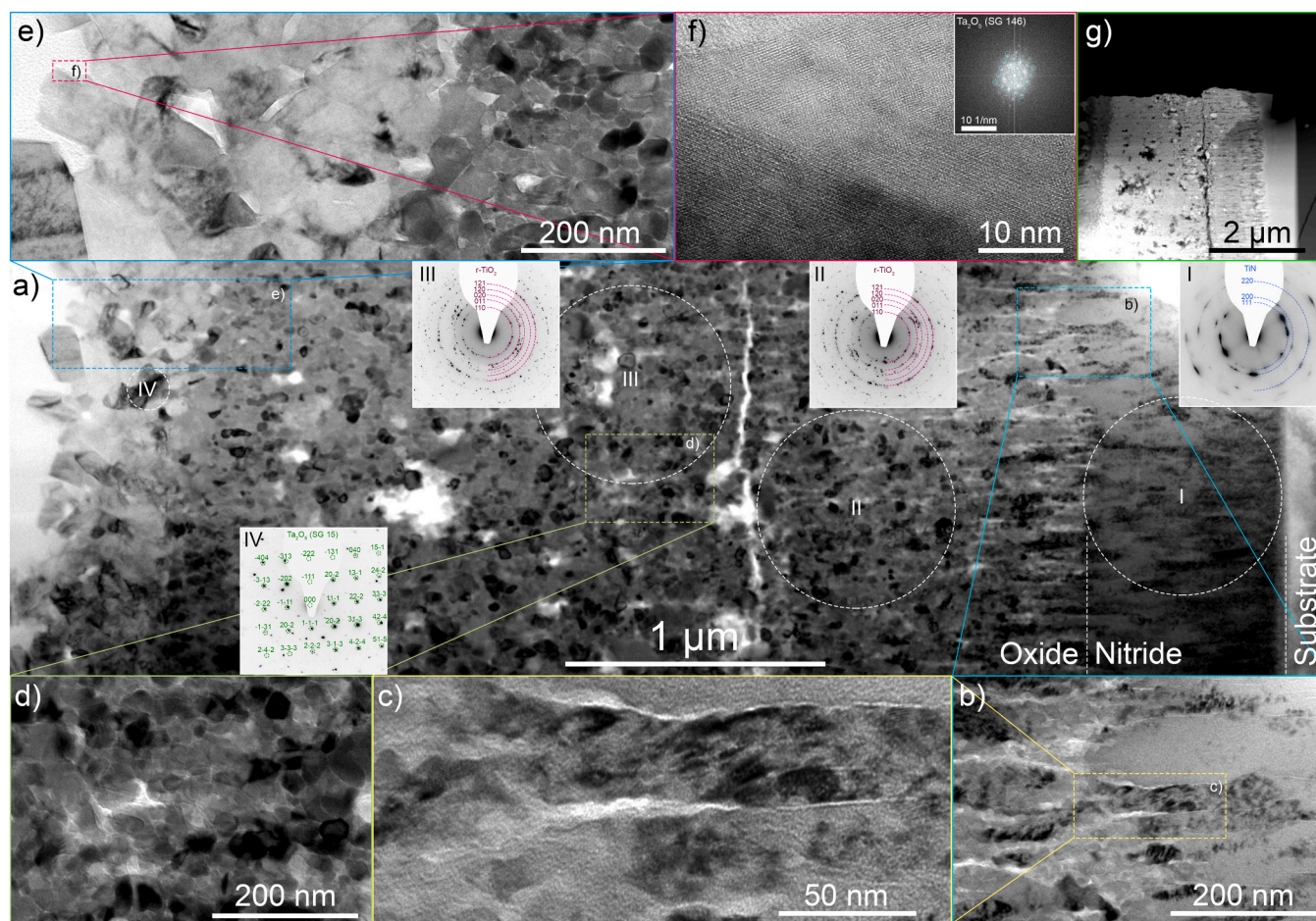


**Fig. 4.** Bright-field TEM investigation of the sample with 6.4 at% Si after 100 h oxidation at 1000 °C. a) shows an overview over the whole oxide scale, b)-f) magnified views from different parts of the oxide scale, marked by dashed boxes. The inset in f) shows an FFT from the bottom left region in f). Electron diffraction patterns were recorded from the circled areas with corresponding labels. g) shows a STEM overview of the sample.

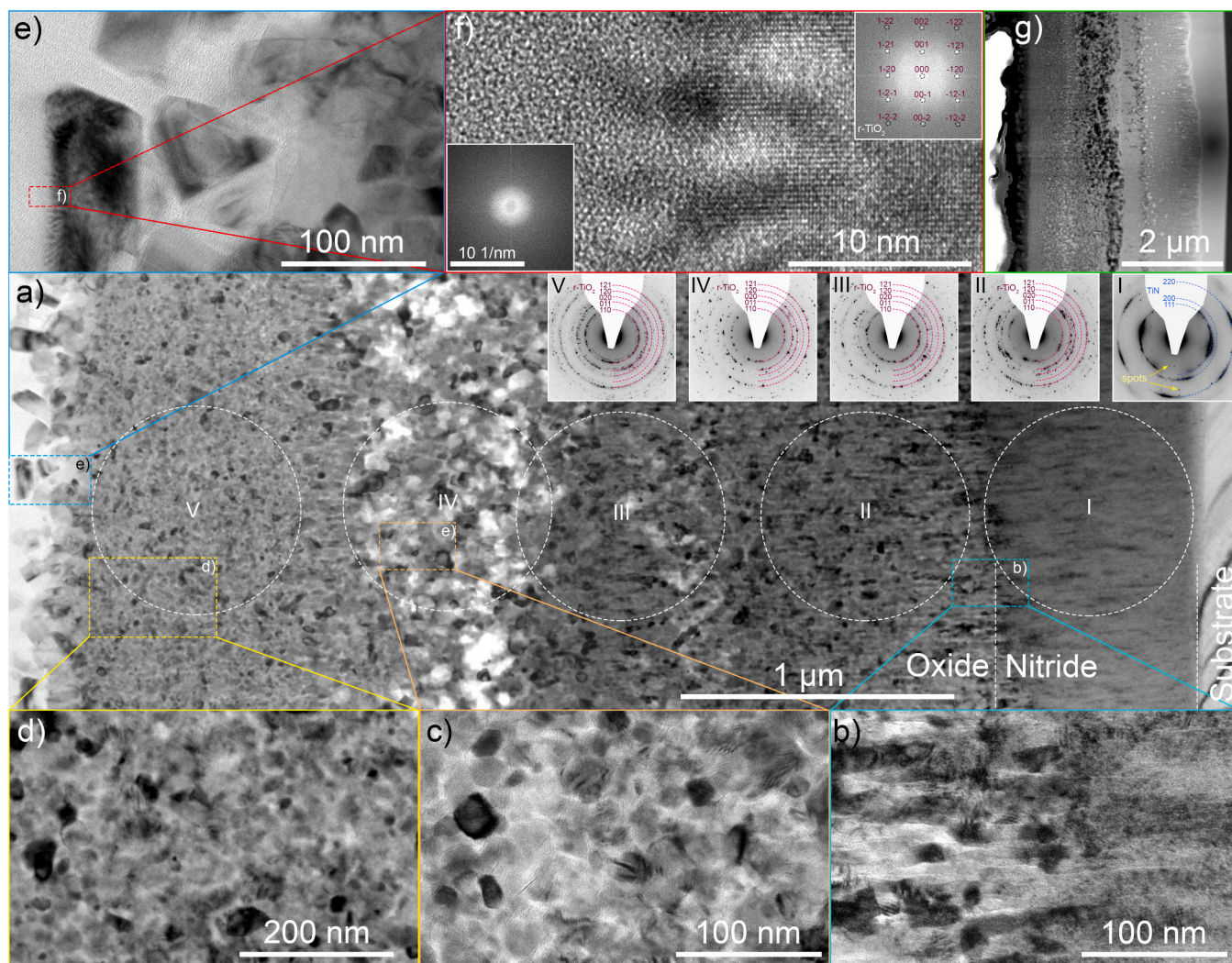
oxide scale starts, which is not as dense anymore as the nitride. Since the sample was prepared as a flat focused ion beam (FIB) lamella, the darker regions within the central oxide scale are pores (e.g. Kirkendall voids), indicating out-diffusion of the elements, so that the oxide scale grows at the outer edge. Towards this outer region, lighter elements accumulated, giving the darker contrast. The amorphous carbon beyond gives the black fringe in the upper left corner of the lamella.

Fig. 5 presents the TEM study of the sample with 9.8 at% Si, with a bright-field overview of the whole cross-section given in Fig. 5a) (again with the substrate to the right). The nitride layer is roughly as thick (780 nm) as in the sample with 6.4 at% Si, but here the columns are much finer due to the higher Si content, in agreement with studies of TiN-Si<sub>3</sub>N<sub>4</sub> coatings [14]. The SAED from area I reveals mostly the fcc structure, but a few scattered spots also hint at a second phase forming after the long exposure to the high temperature, showing limits in the stability of the fcc phase. Details of the interface region between nitride and oxide scale, Fig. 5b), again show that the initial part of the oxide resembles the columnar structure of the nitride with column diameters in the range between 10 and 20 nm. This part of the oxide features mostly a rutile structure again, see the SAED from area II. Despite the morphological changes across the oxide scale, this structure stays dominant also in the other regions III, IV, and V. Only the outermost region V features a prominent second phase, clearly evident by the ring inside the (110) ring of the rutile structure. This is presumably again a Ta<sub>2</sub>O<sub>5</sub> type phase. Although a silicide phase as discussed for the XRD results (Fig. 1) could also fit this pattern, this is less plausible given the proximity to the oxygen-exposed surface.

The morphology of the oxide scale shows a decent change from the interface to the nitride towards its outer surface. For this sample, the columnar oxide grains extend further towards the surface than compared with the sample with 6.4 at% Si, before converting to equiaxed grains. This transition is within the marked area III, before the sublayer with reduced density (area IV) evolves, which is visible by the bright and dark patches in the bright-field and STEM image, respectively. The magnified view of this region, Fig. 5c), shows equiaxed grains with diameters of around 20 nm. Beyond this low-density region, a region composed of lighter elements forms (as suggested by the contrast). The grain size is smaller here with < 10 nm, see the detail in Fig. 5d), which might be a consequence of the formation of the second oxide phase, as indicated by the SAED from this region V, so that two competing phases hinder their grain growth mutually.

At the very top of the oxide scale, again very large grains, 60–120 nm long, are present, forming a rough surface. The magnified view of this region, Fig. 5e), with a high-resolution image from one such grain, Fig. 5f), indicates through the FFT (shown in the top-right inset), that these grains are rutile structured. Beyond these, again amorphous carbon is present, see the FFT in the bottom-left inset. The STEM overview in Fig. 5g) confirms these observations.

The TEM bright-field overview of the oxidized coatings with 15.0 at% Si, Fig. 6a), shows, as noted in the SEM image (Fig. 2), that more than half of the nitride is still present even after 100 h oxidation at 1000 °C. This nitride is even more fine-grained than the other coatings, so that no columnar microstructure is visible at all. The SAED from area I shows a single fcc phase with a strong (200) texture in growth direction. For this



**Fig. 5.** Bright-field TEM investigation of the sample with 9.8 at% Si after 100 h oxidation at 1000 °C. a) shows an overview over the whole oxide scale, b)-f) magnified views from different parts of the oxide scale, marked by dashed boxes. Insets in f) show FFTs from the left and right regions in f). Electron diffraction patterns were recorded from the circled areas with corresponding labels. g) shows a STEM overview of the sample.

sample, the interface between nitride and growing oxide is much sharper compared to the others with no large columns transitioning across their length. The first 200 nm of the oxide scale are composed only of fine equiaxed grains, after which the grain structure becomes more columnar, see also the higher magnification in Fig. 6b). The additional high-resolution image, Fig. 6c), shows equiaxed grains of 10 nm diameter and below. The SAED from area II indicates a dominant rutile phase structure and a second phase that is strongly textured in growth direction. Thus, the columnar grains in the oxide might stem from this second phase.

Towards the surface of the coating on the left end in Fig. 6b) the grains become much larger, forming elongated grains that are 50–70 nm long. The SAED from area III shows that next to the rutile structure, the same textured additional phase like in region II is present, but also an amorphous phase (as suggested by the diffuse dark region in the center of the SAED that spans up to the (110) ring of the rutile structure). The latter is likely a grain boundary phase, because towards the left end of Fig. 6b) bright boundaries around the grains are present, indicating a lack of diffraction contrast. Beyond this region, again a sublayer with fine grains forms, followed by a rough surface formed by large grains that are embedded in amorphous carbon from the sample preparation, see the details in Fig. 6d) and e). The SAED patterns recorded from areas IV and V show a rutile structure. The STEM overview in Fig. 6f) confirms

the much higher density in this oxide scale compared to the previous samples. We also see that the succession of layers corresponding to SAED regions III, IV, and V is accompanied by a decrease in atomic mass.

To further extract information of the oxide scale growth mechanisms, STEM-EDS linescans across the scales are conducted and presented for the samples with 6.4, 9.8, and 15.0 at% Si in Fig. 7a), b), and c), respectively. Additional elemental maps of the surface-near region from the cross-sections are given to the left of the linescans. The major challenge in this analysis is the coincidence of the Si-L edge with the Ta-M edge, due to which we cannot separate these two elements reliably by EDS. Since Ta is much heavier with a higher fluorescence yield, this means that the Si content is vastly overestimated wherever Ta is present. The same is true to a lesser extent for Ti and N, therefore the N signal in the EDS maps (which overlap with the Ti signal) is just a measurement artifact. We also see residual O in the remaining nitride layers, this is a measurement artifact as well since we are measuring on thin TEM lamella. Between sample preparation and measurement these samples were exposed to air and thus oxidized on the surface. Due to the thin samples, the oxidized region represents a significant portion of the total sample volume. Therefore, all regions of the sample appear to contain some O. We applied a correction for this effect in the EDAX software, but this cannot eliminate the problem completely. EELS as complementary spectroscopy is not viable here because of the large number of elements



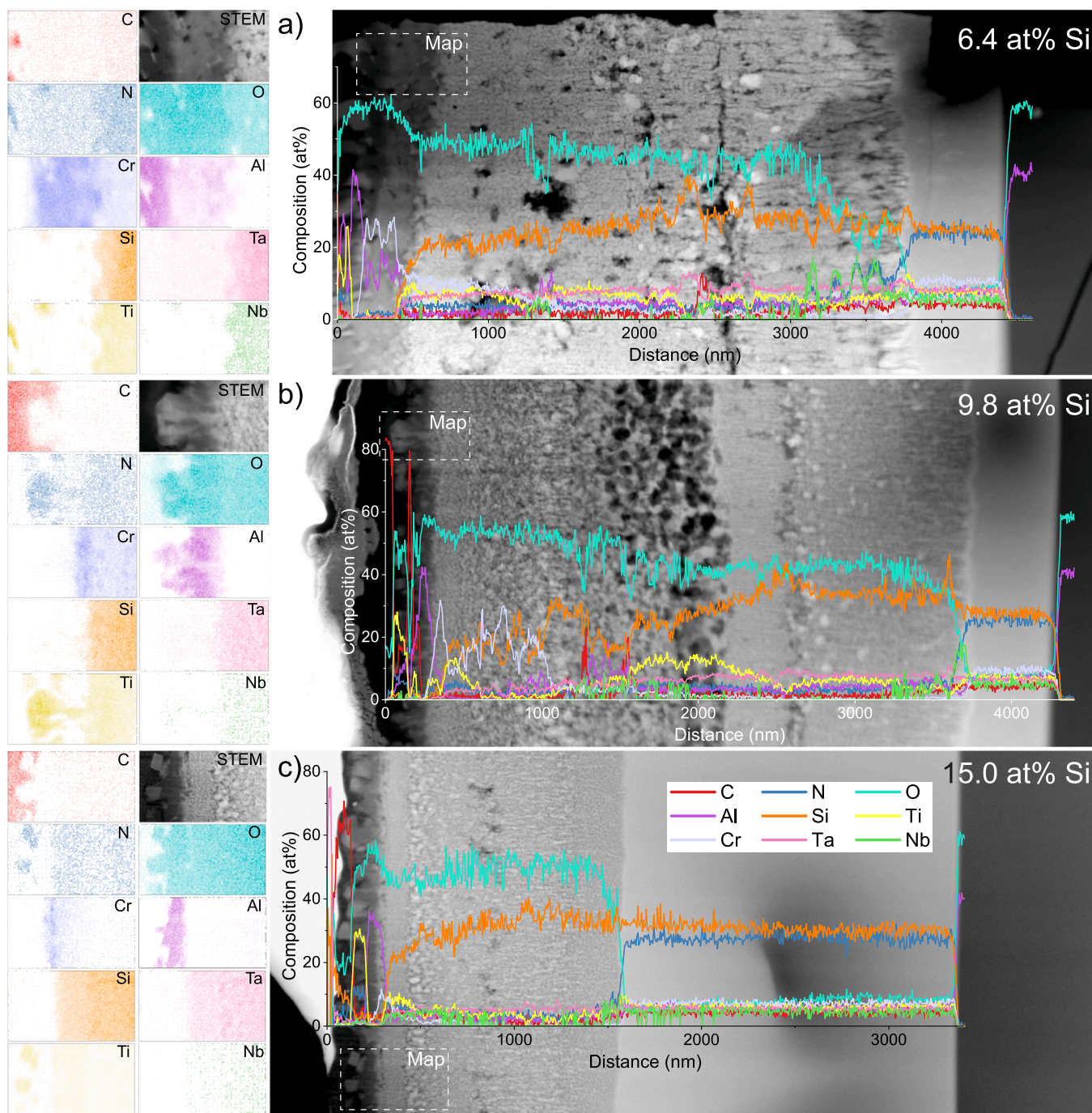


**Fig. 7.** STEM images of the coatings with 6.4 a), 9.8 b), and 15.0 at% Si c) oxidized at 1000 °C for 100 h, with added EDS-linescans and EDS mapping (left) from the dashed box regions. N and Si quantification are affected by the heavier Ti and Ta due to overlapping excitation edge energies.

porous regions during sample preparation. Beyond this porous region, the oxide is Cr-rich to be followed by an Al-rich outer layer. Again, at the very surface, the Ti and C signals spike. The EDS map shows similarly as for the previous sample, that the inner oxide region is rich in Ta and Nb. Cr is concentrated in a thin layer underneath the outermost, Al-rich region. Inside this Al layer a thin Ti-rich channel perpendicular to the surface suggests that a large Ti-oxide broke through, which is surrounded by the C matrix.

For the sample with 15.0 at% Si, Fig. 7c), a thick nitride layer is present, which is uniform and provides a sharp interface to the oxide scale. The oxide exhibits almost no compositional fluctuation, only in the fine-grained region around 400 nm from the surface the Ti signal slightly increases, followed by Cr. But the intensity of the Cr is much

lower when compared to the other samples. Beyond the Cr-rich layer, an Al-oxide layer is formed, once more followed by Ti-oxide. The map reveals the layered succession of heavy transition metals, Cr, Al, and finally individual Ti grains at the very top, embedded in the C matrix.

This order of Al and Ti at the surface is unexpected when looking at their O-affinities, however, Epifano and Monceau [30] calculated that the oxidation of Ti progresses via a more stable intermediary  $Ti_2O_3$  phase that competes with  $Al_2O_3$ , and is only then subsequently oxidized further to the stable rutile- $TiO_2$ , thus explaining the succession of oxide layers as demonstrated on a Ti-Al alloy. The transition between the  $Ti_2O_3$  and r- $TiO_2$  was calculated to happen around 920 °C, therefore our oxidation experiment ran at a sufficient temperature for this phenomenon to occur as well.

The formation of a Ti-rich layer on top of an Al<sub>2</sub>O<sub>3</sub> layer was also observed for (Ti,Al)N coatings oxidized at 1000 °C [20], and (Ti,Al,Cr)N coatings when oxidized at 900 and 1000 °C, but not at 800 °C [31,32]. In both cases, the Cr significantly improved the oxidation resistance via a dense sub-layer beneath the Al<sub>2</sub>O<sub>3</sub>, despite the out-diffusion of Ti. And also in our earlier study about (Al,Cr,Nb,Ta,Ti,Si)N coatings oxidized at 850 °C no top Ti-rich oxide layer formed [27], further supporting the calculation reported in [30].

For all coatings investigated, no Si can be detected in the outer regions of the oxide scale. This can be explained with the lower O-affinity compared to Al and Ti, but Cr has an even lower affinity and is present in the top region. An additional possible explanation could be the evaporation of Si-oxides from the surface in the presence of humidity [33], because the oxidation treatments were conducted in ambient air (30 % relative humidity at 20 °C). In any case, based on the decreased porosity in the oxide scale of the sample with 15.0 at% Si, and the thinner top layers of Al- and Cr-oxide suggest that the improved oxidation resistance of this coating stems from the amorphous grain boundary regions deeper inside the oxide scale, which hinder the out-diffusion of metals to the top of the scale. Thus, protective functionality of the scale is not simply governed by the outer dense Al<sub>2</sub>O<sub>3</sub> and Cr<sub>2</sub>O<sub>3</sub> layers, but also the deeper regions of the oxide scale.

#### 4. Conclusions

Four 2–3 μm thick (Al,Cr,Nb,Ta,Ti,Si)N-based coatings with 0, 6.4, 9.8, and 15.0 at% Si were oxidized at up to 1000 °C for up to 100 h, which represents the harshest isothermal oxidation experiment for crystalline nitride thin films reported. While the Si-free coating succumbed quickly in these environments, all of the Si-alloyed coatings survived the treatment with at least 750 nm of nitride coating left. Detailed investigations of the oxide scales after the 1000 °C test exposed a succession of different microstructures. The best performance is provided by the coating with 15.0 at% Si, which displays the least porosity inside the oxide scale and amorphous grain boundary regions in a part of the oxide scale.

The oxidized Si-free coating crystallizes purely in a rutile structure, while at higher Si contents some Ta<sub>2</sub>O<sub>5</sub>-type phase becomes present as well.

The top-scale reveals a succession of a Ta/Nb/Ti-rich layer followed by Cr, Al, and finally Ti-rich oxides. The presence of the outermost Ti-oxide grains can be explained thermodynamically via an intermediary Ti<sub>2</sub>O<sub>3</sub> phase. Based on the results we can conclude that the amorphous boundary phase present in the oxide scale grown on the 15.0 at% Si containing (Al,Cr,Nb,Ta,Ti)N in combination with a much lower porosity is blocking the out-diffusion of metals. Together these effects allow for an outstanding oxidation resistance of this material.

#### CRedit authorship contribution statement

**Andreas Kretschmer:** Writing – original draft, Visualization, Investigation, Formal analysis, Conceptualization. **Paul Heinz Mayrhofer:** Writing – review & editing, Supervision, Resources, Project administration, Funding acquisition.

#### Declaration of Competing Interest

The authors declare that they have no known competing financial interests or personal relationships that could have appeared to influence the work reported in this paper.

#### Data availability

The data that support the findings of this study are available from the corresponding author upon request.

#### Acknowledgements

This work was funded by the Austrian COMET Program (project K2 In-Tribology, no. 872176). The authors acknowledge the use of the X-ray center (XRC) and USTEM at TU Wien. They are also grateful to Philip Kutrowatz and Tomasz Wojcik (TU Wien, Austria) for TEM sample preparation and analysis, respectively. Plansee Composite Materials GmbH is acknowledged for supplying target materials. The authors acknowledge TU Wien Bibliothek for financial support through its Open Access Funding Programme.

#### Appendix A. Supporting information

Supplementary data associated with this article can be found in the online version at [doi:10.1016/j.jallcom.2024.176912](https://doi.org/10.1016/j.jallcom.2024.176912).

#### References

- [1] K. Mahesh, J.T. Philip, S.N. Joshi, B. Kuriachen, Machinability of Inconel 718: a critical review on the impact of cutting temperatures, *Mater. Manuf. Process.* 36 (7) (2021) 753–791, <https://doi.org/10.1080/10426914.2020.1843671>.
- [2] A. Insektor, P.A. Salvador, Architecture of PVD coatings for metalcutting applications: a review, *Surf. Coat. Technol.* 257 (2014) 138–153, <https://doi.org/10.1016/j.surfcoat.2014.08.068>.
- [3] M. Wittmer, J. Noser, H. Melchior, Oxidation kinetics of TiN thin films, *J. Appl. Phys.* 52 (11) (1981) 6659–6664, <https://doi.org/10.1063/1.328659>.
- [4] L. Chen, J. Paulitsch, Y. Du, P.H. Mayrhofer, Thermal stability and oxidation resistance of Ti-Al-N coatings, *Surf. Coat. Technol.* 206 (11–12) (2012) 2954–2960, <https://doi.org/10.1016/j.surfcoat.2011.12.028>.
- [5] Y.C. Chim, X.Z. Ding, X.T. Zeng, S. Zhang, Oxidation resistance of TiN, CrN, TiAlN and CrAlN coatings deposited by lateral rotating cathode arc, *Thin Solid Films* 517 (17) (2009) 4845–4849, <https://doi.org/10.1016/j.tsf.2009.03.038>.
- [6] Y.-I. Chen, J.-H. Lin, C.-C. Chou, Oxidation resistance and mechanical properties of Ta-Al-N coatings, *Surf. Coat. Technol.* 303 (2016) 41–47, <https://doi.org/10.1016/j.surfcoat.2016.03.022>.
- [7] M. Pfeiler, C. Scheu, H. Hutter, J. Schnöller, C. Michotte, C. Mitterer, M. Kathrein, On the effect of Ta on improved oxidation resistance of Ti-Al-Ta-N coatings, *J. Vac. Sci. Technol. A Vac. Surf. Films* 27 (3) (2009) 554–560, <https://doi.org/10.1116/1.3119671>.
- [8] R. Hollerweger, H. Riedl, M. Arndt, S. Kolozsvári, S. Primig, P. Mayrhofer, Guidelines for increasing the oxidation resistance of Ti-Al-N based coatings, *Thin Solid Films* 688 (2019) 137290, <https://doi.org/10.1016/j.tsf.2019.05.009>.
- [9] M.J. Brova, E. Alat, M.A. Pauley, R. Sherbondy, A.T. Motta, D.E. Wolfe, Undoped and ytterbium-doped titanium aluminum nitride coatings for improved oxidation behavior of nuclear fuel cladding, *Surf. Coat. Technol.* 331 (April) (2017) 163–171, <https://doi.org/10.1016/j.surfcoat.2017.09.076>.
- [10] J. Wang, M.A.P. Yazdi, F. Lomello, A. Billard, A. Kovács, F. Schuster, C. Guet, T. J. White, Y. Wouters, C. Pascal, F. Sanchette, Z. Dong, The Yttrium Effect on Nanoscale Structure, Mechanical Properties, and High-Temperature Oxidation Resistance of (Ti<sub>0.6</sub>Al<sub>0.4</sub>)<sub>1-x</sub>Y<sub>x</sub>N Multilayer Coatings, *Metall. Mater. Trans. A* 48 (9) (2017) 4097–4110, <https://doi.org/10.1007/s11661-017-4187-6>.
- [11] H. Asanuma, F. Klimashin, P. Polcik, S. Kolozsvári, H. Riedl, P. Mayrhofer, Impact of lanthanum and boron on the growth, thermomechanical properties and oxidation resistance of Ti-Al-N thin films, *Thin Solid Films* 688 (February) (2019) 137239, <https://doi.org/10.1016/j.tsf.2019.04.014>.
- [12] H. Asanuma, F.F. Klimashin, P. Polcik, S. Kolozsvári, H. Riedl, P.H. Mayrhofer, Hard Ti-Al-N endowed with high heat-resistance through alloying with Ta and Ce, *Surf. Coat. Technol.* 372 (May) (2019) 26–33, <https://doi.org/10.1016/j.surfcoat.2019.05.018>.
- [13] S.P. Taguchi, S. Ribeiro, Silicon nitride oxidation behaviour at 1000 and 1200 °C, *J. Mater. Process. Technol.* 147 (3) (2004) 336–342, <https://doi.org/10.1016/j.jmatprotec.2004.01.003>.
- [14] S. Veprek, M.G. Veprek-Heijman, The formation and role of interfaces in superhard nc-MenN/a-Si<sub>3</sub>N<sub>4</sub> nanocomposites, *Surf. Coat. Technol.* 201 (13) (2007) 6064–6070, <https://doi.org/10.1016/j.surfcoat.2006.08.112>.
- [15] J. Musil, J. Vlček, P. Zeman, Hard amorphous nanocomposite coatings with oxidation resistance above 1000 °C, *Adv. Appl. Ceram.* 107 (3) (2008) 148–154, <https://doi.org/10.1179/174367508X306460>.
- [16] L. Duan, H. Wu, W. Xiu, X. Yu, L. Guo, High temperature wettability and oxidation behavior of TiN, Ti-Al-N and Ti-Si-N PVD film, *Mater. Res. Express* 7 (11) (2020) 116401, <https://doi.org/10.1088/2053-1591/abc3f4>.
- [17] M.-R. Alhafian, N. Valle, J.-B. Chemin, L. Bourgeois, M. Penoy, R. Useldinger, J. Ghanbaja, F. Mücklich, P. Choquet, Influence of Si addition on the phase structure and oxidation behavior of PVD AlTiN and AlTiCrN coatings using high-resolution characterization techniques, *J. Alloy. Compd.* 968 (August) (2023) 171800, <https://doi.org/10.1016/j.jallcom.2023.171800>.
- [18] I.V. Blinkov, D.S. Belov, A.O. Volkhonsky, V.S. Sergevnin, A.N. Nizamova, A. V. Chernogor, F.V. Kiryukhantsev-Korneev, Heat Resistance, High-Temperature Tribological Characteristics, and Electrochemical Behavior of Arc-PVD Nanostructural Multilayer Ti-Al-Si-N Coatings, *Prot. Met. Phys. Chem. Surf.* 54 (3) (2018) 416–424, <https://doi.org/10.1134/S2070205118030048>.

- [19] C. Tritremmel, R. Daniel, C. Mitterer, P.H. Mayrhofer, M. Lechthaler, P. Polcik, Oxidation behavior of arc evaporated Al-Cr-Si-N thin films, *J. Vac. Sci. Technol. A: Vac., Surf., Films* 30 (6) (2012) 061501, <https://doi.org/10.1116/1.4748802>.
- [20] A. Vennemann, H.-R. Stock, J. Kohlscheen, S. Rambadt, G. Erkens, Oxidation resistance of titanium-aluminium-silicon nitride coatings, *Surf. Coat. Technol.* 174-175 (2003) 408–415, [https://doi.org/10.1016/S0257-8972\(03\)00407-9](https://doi.org/10.1016/S0257-8972(03)00407-9).
- [21] K. Bobzin, T. Brögelmann, N. Kruppe, M. Carlet, Wear behavior and thermal stability of HPPMS (Al,Ti,Cr,Si)ON, (Al,Ti,Cr,Si)N and (Ti,Al,Cr,Si)N coatings for cutting tools, *Surf. Coat. Technol.* 385 (January) (2020) 125370, <https://doi.org/10.1016/j.surfcoat.2020.125370>.
- [22] M. Nussbaum, M. Arab Pour Yazdi, A. Michau, E. Monsifrot, F. Schuster, H. Maskrot, A. Billard, Mechanical properties and high temperature oxidation resistance of (AlCrTiV)N coatings synthesized by cathodic arc deposition, *Surf. Coat. Technol.* 434 (February) (2022) 128228, <https://doi.org/10.1016/j.surfcoat.2022.128228>.
- [23] S. Liu, C. Liu, Z. Yang, L. He, G. Zeng, W. Zhang, J. Long, H. Chang, Microstructure, high-temperature corrosion resistance and oxidation properties of (TiVZrCrAl)N high entropy nitride coatings with different N<sub>2</sub>/Ar ratios, *Surf. Coat. Technol.* 476 (August 2023) (2024) 130226, <https://doi.org/10.1016/j.surfcoat.2023.130226>.
- [24] A. Bouissil, S. Achache, D.E. Touaibia, B. Panicaud, M.A.P. Yazdi, F. Sanchette, M. El Garah, Properties of a new TiTaZrHfW(N) refractory high entropy film deposited by reactive DC pulsed magnetron sputtering, *Surf. Coat. Technol.* 462 (November 2022) (2023) 129503, <https://doi.org/10.1016/j.surfcoat.2023.129503>.
- [25] D.E. Touaibia, S. Achache, A. Bouissil, J. Ghanbaja, S. Migot, M.A.P. Yazdi, F. Schuster, B. Panicaud, F. Sanchette, M. ElGarah, Oxidation resistance and mechanical properties of AlTiZrHfTa(-N) high entropy films deposited by reactive magnetron sputtering, *J. Alloy. Compd.* 969 (September) (2023) 172397, <https://doi.org/10.1016/j.jallcom.2023.172397>.
- [26] W.J. Shen, M.H. Tsai, K.Y. Tsai, C.C. Juan, C.W. Tsai, J.W. Yeh, Y.S. Chang, Superior oxidation resistance of (Al<sub>0.34</sub>Cr<sub>0.22</sub>Nb<sub>0.11</sub>Si<sub>0.11</sub>Ti<sub>0.22</sub>)<sub>50</sub>N<sub>50</sub> high-entropy nitride, *J. Electrochem. Soc.* 160 (11) (2013) 531–535, <https://doi.org/10.1149/2.028311jes>.
- [27] A. Kretschmer, A. Kirnbauer, V. Moraes, D. Primetzhofer, K. Yalamanchili, H. Rudigier, P.H. Mayrhofer, Improving phase stability, hardness, and oxidation resistance of reactively magnetron sputtered (Al,Cr,Nb,Ta,Ti)N thin films by Si-alloying, *Surf. Coat. Technol.* 416 (February) (2021) 127162, <https://doi.org/10.1016/j.surfcoat.2021.127162>.
- [28] C.M. Koller, R. Hollerweger, C. Sabitzer, R. Rachbauer, S. Kolozsvári, J. Paulitsch, P.H. Mayrhofer, Thermal stability and oxidation resistance of arc evaporated TiAlN, TaAlN, TiAlTaN, and TiAlN/TaAlN coatings, *Surf. Coat. Technol.* 259 (PC) (2014) 599–607, <https://doi.org/10.1016/j.surfcoat.2014.10.024>.
- [29] C.M. Koller, A. Kirnbauer, R. Rachbauer, S. Kolozsvári, P.H. Mayrhofer, Thermally-induced phase transformation sequence of arc evaporated Ta-Al-N coatings, *Scr. Mater.* 113 (2016) 75–78, <https://doi.org/10.1016/j.scriptamat.2015.09.040>.
- [30] E. Epifano, D. Monceau, Ellingham diagram: A new look at an old tool, *Corros. Sci.* 217 (March) (2023) 111113, <https://doi.org/10.1016/j.corsci.2023.111113>.
- [31] M. Danek, F. Fernandes, A. Cavaleiro, T. Polcar, Influence of Cr additions on the structure and oxidation resistance of multilayered TiAlCrN films, *Surf. Coat. Technol.* 313 (2017) 158–167, <https://doi.org/10.1016/j.surfcoat.2017.01.053>.
- [32] X. Sui, G. Li, H. Zhou, S. Zhang, Y. Yu, Q. Wang, J. Hao, Evolution behavior of oxide scales of TiAlCrN coatings at high temperature, *Surf. Coat. Technol.* 360 (January) (2019) 133–139, <https://doi.org/10.1016/j.surfcoat.2019.01.016>.
- [33] E.J. Opila, R.E. Hann, Paralineer oxidation of CVD SiC in water vapor, *J. Am. Ceram. Soc.* 80 (1) (1997) 197–205, <https://doi.org/10.1111/j.1151-2916.1997.tb02810.x>.